

# **Electrochemical behavior of nanostructured NiO@C anode in a lithium-ion battery using $\text{LiNi}_{1/3}\text{Co}_{1/3}\text{Mn}_{1/3}\text{O}_2$ cathode**

Shuangying Wei<sup>a,†</sup>, Daniele Di Lecce<sup>b,†</sup>, Rosaria Brescia<sup>c</sup>, Giammarino Pugliese<sup>c</sup>, Paul R.

Shearing<sup>b</sup>, Jusef Hassoun<sup>a,d,\*</sup>

<sup>a</sup> *Department of Chemical and Pharmaceutical Sciences, University of Ferrara, Via Fossato di Mortara, 17, 44121, Ferrara, Italy.*

<sup>b</sup> *Electrochemical Innovation Lab, Department of Chemical Engineering, University College London, Torrington Place, London, WC1E 7JE, United Kingdom*

<sup>c</sup> *Istituto Italiano di Tecnologia (IIT), Via Morego 30, 16163 Genova (Italy)*

<sup>d</sup> *National Interuniversity Consortium of Materials Science and Technology (INSTM), University of Ferrara Research Unit, University of Ferrara, Via Fossato di Mortara, 17, 44121, Ferrara, Italy.*

<sup>†</sup> Authors equally contributed

\* Corresponding authors: [jusef.hassoun@unife.it](mailto:jusef.hassoun@unife.it).

## **Abstract**

A NiO@C composite anode is prepared through an alternative synthesis route involving precipitation of a carbon precursor on NiO nanopowder, annealing under argon to form a Ni core, and oxidation at moderate temperature to get metal oxide particles whilst retaining carbon and metallic Ni in traces. The electrode reversibly reacts in lithium cells by the typical conversion process occurring in a wide potential range with the main electrochemical activity at 1.3 V vs.  $\text{Li}^+/\text{Li}$  during discharge and at 2.2 V vs.  $\text{Li}^+/\text{Li}$  during charge. The NiO@C material exhibits highly improved behavior in a lithium half-cell compared to bare NiO due to faster electrode kinetics and superior stability over electrochemical displacement, leading to a reversible capacity approaching

800 mAh g<sup>-1</sup>, much enhanced cycle life and promising rate capability. The applicability of the NiO@C anode is further investigated in a lithium-ion NiO@C/LiNi<sub>1/3</sub>Co<sub>1/3</sub>Mn<sub>1/3</sub>O<sub>2</sub> cell, which operates at about 2.5 V delivering about 160 mAh g<sup>-1</sup> with respect to the cathode mass. The cell exhibits stable response upon 80 cycles at a C/2 rate with coulombic efficiency ranging from 97% to 99%.

**Keywords:** Conversion anode; NiO; Nanoparticles; Electrochemical Impedance Spectroscopy; Lithium-ion battery; LiNi<sub>1/3</sub>Co<sub>1/3</sub>Mn<sub>1/3</sub>O<sub>2</sub>.

## Introduction

Lithium-ion batteries (LIBs) are largely employed in portable electronics and electric vehicles by virtue of intriguing characteristics in terms of energy density and cycle life as well as high coulombic and energy efficiency [1,2]. Since the first reports on the “*rocking-chair*” concept in 1980 [3] and the following commercialization in 1991, the energy density has been gradually increased up to values exceeding 200 Wh kg<sup>-1</sup> by developing alternative electrode and electrolyte chemistries with tailored morphological features whilst simultaneously improving the cell design [4]. As for the cathode, the layered LiCoO<sub>2</sub> extensively employed in the first commercial configurations, has been progressively replaced by advanced layered compounds comprising various metals in order to mitigate the environmental concerns due to the use of cobalt and boost the gravimetric capacity above 140 mAh g<sup>-1</sup>. In this respect, LiNi<sub>1/3</sub>Co<sub>1/3</sub>Mn<sub>1/3</sub>O<sub>2</sub> (NCM) and LiNi<sub>0.8</sub>Co<sub>0.15</sub>Al<sub>0.05</sub>O<sub>2</sub> (NCA) have demonstrated remarkable performance leading to a widespread proliferation after launch onto the market [4]. As for the anode, commercial graphite has suitable properties in terms of working voltage and capacity, benefiting from a reversible Li<sup>+</sup> intercalation process exchanging about 0.17 lithium equivalents per C unit below 0.1 V vs. Li<sup>+</sup>/Li [5]. However, a great deal of research has so far been devoted to various alternative electrode materials exhibiting a higher Li<sup>+</sup> uptake at relatively low voltage, such as lithium alloys and transition metal oxides,

which might significantly increase the anode reversible capacity with respect to the active material from 372 mAh g<sup>-1</sup> to values above 600 mAh g<sup>-1</sup> [6–8]. In particular, nanosized metal oxides with chemical formula M<sub>x</sub>O<sub>y</sub> (where M is typically a transition metal) may reversibly react in lithium cells by a multi-electron conversion mechanism leading to the formation of M<sup>0</sup> nano-domains embedded into a Li<sub>2</sub>O matrix [9]. Accordingly, nickel oxide (NiO) may be electrochemically reduced to metallic Ni and Li<sub>2</sub>O delivering 718 mAh g<sup>-1</sup> [10]. Other oxides, such as SiO<sub>2</sub>, may exhibit a large capacity (above 800 mAh g<sup>-1</sup>), superior rate capability, and remarkable cycling stability [11]. Transition metal sulfides have similar characteristics as conversion anodes in terms of capacity, however they suffer from the typical drawbacks of conversion electrodes [12]. Hence, in spite of the attractive capacity, the conversion reaction is characterized by massive microstructural rearrangements [13] mostly leading to substantial volume changes of the electrode material and large voltage hysteresis, which may adversely affect the reversibility and efficiency of the process [9]. Furthermore, they typically show a higher working voltage than graphite and Li-alloying anodes [9,14]. The severe electrode reorganization may cause pulverization and loss of electric contact of the active material which are reflected as rapid capacity fade, while the voltage signature may limit the effective use in full lithium-ion cells due to relatively low operating voltage and gradual electrode unbalancing during cycling [5]. Furthermore, a huge irreversible capacity loss of conversion electrodes typically occurring upon the first cycle requires anode pre-lithiation strategies which further hinder commercialization [15]. Therefore, electrochemical studies suitably combining material optimization in terms of structure and morphology, investigation in half-cells, and full-cell demonstration are considered crucial for this class of materials [4,5].

Nanostructures may mitigate the expansion of conversion materials upon discharge and increase the active surface [16], while incorporation into carbon matrices of various morphologies may enhance the conductivity and buffer volume variations [17]. Thus, nanomembranes [18],

nanofibers [19], nanowires [20], and nanobelts [21] have revealed promising performances even at a high current density. However, the nanostructure might trigger undesired side reactions leading to deterioration of the electrode/electrolyte interphase upon long-term cycling [22]. Therefore, a careful tuning of the morphological features of metal oxide-carbon composites and carbon-coated metal oxide electrodes ( $M_xO_y@C$ ) is a key requirement to effectively enhance the conversion reaction whilst limiting possible parasitic processes [23,24]. Indeed, long cycling performance has been demonstrated for NiO/MWCNT electrodes [25], NiO/C nanocapsules [26] and NiO core-shell nanocables [27]. Further improvements might be achieved by developing simple synthetic approaches to get nanostructured metal oxide composites [28]. Fine electrode engineering may buffer the volume changes of NiO upon electrochemical conversion, despite possible penalties in terms of gravimetric energy density due to the low capacity of electron-conductive carbon additives, which are typically employed to improve rate capability and cycle life. Following this trend, NiO anodes exploiting carbon of various nature have been widely investigated in recent reports demonstrating promising electrode performances in lithium-half cells [29–37]. Reduced graphene oxide (r-GO) has suitable properties for preparing NiO-based composite electrodes. Accordingly, hollow carbon fibers hosting about 35 wt.% of NiO nanoparticles wrapped by r-GO exhibited enhanced reversible capacity, rate capability, and cycling stability [29]. A comparative study of NiO-based composites containing rGO at various oxidation degrees has shown that the functional groups on rGO affect the cycling behavior in lithium-half cells [35]. On the other hand, NiO trapping in hollow carbon structures and/or nanotubes as well as graphene papers may mitigate the electrode degradation and improve the cycle life [36–38], while core-shell morphologies may lead to a remarkable specific capacity [31]. Large capacity in lithium half-cell can be also ensured by depositing NiO nanoparticles on N-doped carbon sheets arranged into hollow spheres [32]. Furthermore, fibrous microstructures with suitable features for battery applications have been prepared either by employing a rod-like

precursor in the NiO synthesis [33] or by coating carbon fibers with N-doped carbon, NiO and carbon dots to obtain a free-standing, flexible electrode [39]. An effective decrease in C content in the composite down to 1 wt.% has been demonstrated in a recent report on NiO hexagonal platelets exhibiting much enhanced performances compared to those of bare NiO platelets with circular morphology [34]. Interestingly, hollow Ni/NiO nanospheres embedded in graphite sheets have been prepared by polymerization of a carbon precursor in presence of a nickel salt, pyrolysis at 800 °C to form metallic nickel embedded in a carbon matrix, and subsequent oxidation at 350 °C [30]. However, only a few works investigated the actual behavior of NiO anodes in lithium-ion cells [38–40] despite the great amount of literature on the conversion-anode performance in half-cell configuration [18–21,24–27,41,42], even though a detailed investigation in the full cell employing a conventional cathode, such as NCM, is considered to be essential to assess the actual applicability [4,43], particularly considering the abovementioned issues in terms of electrode stability upon cycling, working voltage and coulombic efficiency [9]. Therefore, we study herein, a NiO anode in a lithium-ion battery using the high-performance NCM layered cathode. Structure, morphology and composition are carefully controlled by a two-step method involving carbon precipitation on metal-oxide nanoparticles in a reducing environment followed by oxidation at moderate temperature. The anode conversion process in the cell is characterized by performing voltammetry, impedance spectroscopy and galvanostatic measurements, thereby revealing promising behavior for possible applications. Hence, this comparative study interestingly reveals how the anode electrochemistry may affect the characteristics of the lithium-ion battery in terms of working voltage, coulombic efficiency and cycling stability. Furthermore, electrochemical measurements performed with the support of a lithium reference electrode shed light on the effect of anode and cathode features on the full cell, thus elucidating the role played by a suitable electrode balancing.

## **Experimental**

2 g of NiO (Sigma-Aldrich, <50 nm) was suspended in a water/ethanol solution (50 mL, 1:1 v/v). 4 g of sucrose was added to the above-mentioned suspension and the solvent was evaporated at 70 °C under stirring. The dry mixture was heated at 120 °C for 10 h and at 600 °C for 3 h under an argon flow to obtain Ni@C (step 1). Afterwards, the samples were heated at 380 °C for 48 h under a dry air flow to get NiO@C (step 2). Steps 1 and 2 were carried out in a tubular furnace (GHA, Carbolite) using a 5 °C min<sup>-1</sup> heating rate and natural cooling. Figure 1 depicts the sucrose addition to bare NiO followed by pyrolysis (step 1) and the subsequent mild oxidation of the Ni@C intermediate to form the NiO@C material (step 2).

### Figure 1

Sample structure was investigated by X-ray diffraction (XRD) through a Bruker D8 Advance (Cu K $\alpha$ ) by performing scans from 20 to 90° with step size of 0.02° at 10 s step<sup>-1</sup>. Rietveld refinement of the diffraction pattern of NiO@C was carried out through the MAUD software [44] by using reference structures with cubic unit cell and  $Fm\bar{3}m$  space group (ICSD # 260169 and # 9866) for NiO and Ni. The atom occupancies for the NiO phase have been fixed to the stoichiometric values, and the atomic displacement parameters have been forced to have the same value for each element. Lattice parameters, crystallite size and crystal phase ratio were refined to get suitable weighted-profile (Rwp%) and goodness-of-fit ( $\sigma$ ) values (see Table 1).

### Table 1

A thermogravimetric analysis (TGA) of was performed under an air flow (50 mL min<sup>-1</sup>) by heating a NiO@O sample from 30 to 800 °C at a rate of 10 °C min<sup>-1</sup> through a TGA Q500 from TA instruments. Morphology, structure and elemental composition were studied by scanning electron microscopy (SEM), SEM-energy dispersive X-ray spectroscopy (SEM-EDS), high-angle annular dark-field scanning transmission electron microscopy (HAADF-STEM), energy-filtered TEM (EFTEM), high-resolution TEM (HRTEM), and electron energy-loss spectroscopy (EELS). SEM and SEM-EDS were performed by means of a Zeiss EVO MA10 microscope employing a

tungsten thermionic electron gun and an INCA X-ACT Oxford Instrument analyzer. Each sample for TEM (NiO, Ni@C and NiO@C) was prepared by suspending a spatula tip in ethanol and mildly sonicating; afterwards, the supernatant was drop-cast onto a holey amorphous carbon film on Cu grid. The TEM analyses were carried out on a JEOL JEM-2200FS microscope (Schottky emitter), operated at 200 kV, equipped with a CEOS corrector for the objective lens and an in-column image filter ( $\Omega$ -type). EFTEM imaging was used to acquire elastically-filtered (zero-loss, ZL) TEM images, by selecting only electrons within 10 eV from the ZL peak, and for elemental mapping, carried out by using the three-windows method at the K edge of C (16 eV slit width) and O (20 eV slit width) and at the  $L_{23}$  edge of Ni (30 eV slit width). EEL spectra were acquired on regions of the samples suspended on holes in the support film, in diffraction mode ( $\alpha = 3.5$  mrad,  $\beta = 5.4$  mrad). EELS-based quantification was performed employing the hydrogenic model for all edges (K edge of C and O and  $L_{23}$  edge of Ni), with the background fit in a 30 eV window before the edge and 70 eV window from the edge onset.

Each anode powder (*i.e.*, bare NiO, Ni@C, and NiO@C) was mixed with polyvinylidene fluoride (PVDF 6020, Solvay) and Super P carbon (Timcal) in the 8:1:1 weight ratio. The mixture was dispersed in N-methyl pyrrolidone (NMP, Sigma-Aldrich) and cast on a copper foil through a doctor blade. The cast slurry was heated for 3 h at 70 °C on a hot plate under a fume hood and then dried overnight under vacuum at 110 °C. The anode materials (*i.e.*, bare NiO, Ni@C, and NiO@C) had a mass loading over the electrodes ranging from 1.5 to 2.5 mg cm<sup>-2</sup>. Disks with diameter of 10 and 14 mm were cut out from these dried foils and employed as working electrodes in three-electrode and two-electrode cells (T-type; 10 mm) and CR2032 coin-cells (MTI Corporation; 14 mm), as well as counter electrode in two-electrode full-cells (T-type; 10 mm).

NCM, polyvinylidene fluoride (PVDF 6020, Solvay), and Super P carbon (Timcal) were mixed in the 8:1:1 weight ratio in N-methyl pyrrolidone (NMP, Sigma-Aldrich) and cast on an aluminum foil through a doctor blade. The cast slurry was heated for 3 h at 70 °C on a hot plate

under a fume hood and then dried overnight under vacuum at 110 °C. The NCM electrodes had an active mass loading ranging from 3.1 and 3.5 mg cm<sup>-2</sup>. Disks with diameter of 10 mm were cut out from this electrode sheet and employed as working electrodes in two-electrode, lithium-ion cells. The cells were assembled in an Ar-filled glovebox (H<sub>2</sub>O and O<sub>2</sub> content below 1 ppm, MBRAUN). Lithium metal disks were used as counter and reference electrodes. Lithium-ion batteries were assembled by coupling a NiO@C anode (between 1.7 and 2.3 mg cm<sup>-2</sup>) and an NCM cathode (between 3.1 and 3.6 mg cm<sup>-2</sup>) in T-type two-electrode cell, as well as in a T-type three-electrode cell. The anode was electrochemically activated as reported below. The cell separator (Whatman glass fiber, GF/A) was soaked by an electrolyte solution formed of lithium hexafluorophosphate (LiPF<sub>6</sub>, 1 M) in a mixture (1:1 w/w) of ethylene carbonate (EC) and dimethyl carbonate (DMC).

Cyclic voltammetry (CV) and electrochemical impedance spectroscopy (EIS) measurements were performed on three-electrode half-cells (T-type) through a VersaSTAT MC Princeton Applied Research (PAR, AMETEK) multichannel potentiostat. CV was carried out by using a scan rate of 0.1 mV s<sup>-1</sup> within the potential range from 0.01 to 2.8 V vs. Li<sup>+</sup>/Li. Impedance spectra were recorded at the open circuit voltage (OCV) condition and after 1, 2 and 3 full discharge/charge voltammetry cycles by applying an alternate voltage signal with amplitude of 10 mV in the frequency range from 500 kHz to 100 mHz.

Cycling tests of the NiO@C electrode were performed on two-electrode half-cells (CR2032 coin-cells, MTI Corporation) at a C/5 rate (1C = 718 mA g<sup>-1</sup>). Furthermore, the electrode rate capability was evaluated by galvanostatic cycling in lithium coin-cells (CR2032 coin-cells, MTI Corporation) with current rates of C/10, C/8, C/5, C/3, C/2, 1C, 2C increasing every 5 cycles and decreasing to C/10 at the 36<sup>th</sup> cycle. The voltage window of the galvanostatic measurements was 0.01 to 2.8 V.

Prior to the NiO@C/NCM full-cell assembly, the anode was activated by 3 discharge/charge cycles at a C/5 rate in a T-type, two-electrode half-cell within the 0.01 – 2.8 V range with final charge up to 2.2 V. Afterwards, the electrochemically-activated NiO@C electrode was recovered from the cell, rinsed with DMC to remove electrolyte traces, dried under vacuum for few minutes, and used to build the full-cell. A two-electrode NiO@C/NCM cell was cycled at a C/2 rate (where 1C is 170 mA g<sup>-1</sup> as referred to the positive electrode) within the voltage range from 0.8 to 4.3 V. A three-electrode NiO@C/NCM cell employing a lithium-metal reference probe was cycled at a C/2 rate (where 1C is 170 mA g<sup>-1</sup> as referred to the positive electrode) within a voltage range between the NiO@C and NCM electrodes of 0.8 – 4.3 V, namely. The potential vs. Li<sup>+</sup>/Li of NiO@C and NCM during two-electrode cycling was measured by the abovementioned lithium-metal probe. EIS measurements were carried on t NiO@C/NCM cell at the OCV and after the 1<sup>st</sup>, 10<sup>th</sup>, 50<sup>th</sup>, and 80<sup>th</sup> cycle (after charging) by applying an alternate voltage signal of 10 mV within the frequency range from 500 kHz to 20 mHz. The impedance spectra were analyzed by a nonlinear least squares (NLLS) procedure the spectra. Further EIS measurements Li/NiO@C and Li/NCM sides of the full cell were carried out by using the lithium-metal probe, and applying an alternate voltage signal of 10 mV within the frequency range from 500 kHz to 20 mHz. These EIS analyses were performed through a VersaSTAT MC Princeton Applied Research (PAR, AMETEK) multichannel potentiostat. A rate capability test was carried out on the NiO@C/NCM cell by galvanostatic cycling within the current range from C/5 to 2C rates (where 1C is 170 mA g<sup>-1</sup> as referred to the positive electrode) and the voltage range between NiO@C and NCM of 0.8 – 4.3 V. Furthermore, the potential vs. Li<sup>+</sup>/Li of NiO@C and NCM during above cycling was monitored by using the lithium-metal probe.

All the galvanostatic cycling measurements were carried out by means of a Maccor Series 4000 Battery system. All the electrochemical tests were performed at room temperature.

## **Results and Discussion**

The structural evolution of the composite electrode during the synthetic steps is reported in Figure 2. The indexed XRD patterns of NiO, Ni@C and NiO@C reveal substantial phase changes promoted by the various treatments, with full reduction of the pristine NiO (ICSD # 9866) to Ni metal (ICSD # 260169) upon annealing in argon atmosphere (step 1), and its subsequent oxidation after mild thermal treatment under air (step 2). Furthermore, the figure evidences that the final NiO@C sample contains NiO as the main phase along with traces of metallic nickel, thus suggesting a partial oxidation during step 2 [45]. The absence of graphite peaks might suggest that the carbon coating produced by sucrose pyrolysis has low crystallinity. We may reasonably suppose that the presence of the lowly crystalline carbon as well as of traces of metallic Ni can suitably increase the electronic conductivity of the electrode material, thus possibly enhancing its electrochemical behavior in lithium cell [45]. A Rietveld refinement of the XRD patterns [44] indicates a Ni metal content in NiO@C of 4 wt.% with regard to the overall weight of the crystalline domains, and crystallite size of about 34 nm for the NiO phase and 140 nm for the Ni one (see Table 1). The patterns of both Ni and NiO have been indexed to reference structures with cubic unit cell and  $Fm\bar{3}m$  space group (ICSD # 260169 and # 9866), despite the known rhombohedral distortion of the NiO crystal lattice at room temperature, which does not affect the X-ray reflections and, therefore, can be neglected in our study [46,47]. A thermogravimetric analysis (TGA) under an air flow (Figure 2b) shows that the NiO@C powder undergoes weight change due to concomitant oxidation of C (weight loss) and Ni (weight increase), thereby leading to a final raise of 0.77% with respect to the initial mass. On the other hand, the Rietveld analysis of the XRD patterns of NiO@C indicates a Ni weight fraction of the crystalline domains of about 0.04 (see Table 1). Therefore, we can estimate a carbon content in NiO@C below 4 wt.% considering the full oxidation of Ni to NiO upon the TGA scan.

## Figure 2

Sample morphology and structure has been thoroughly investigated by SEM, HRTEM, HAADF-STEM and ZL-TEM imaging, along with analyses of the elemental distribution over the samples via SEM-EDS and EFTEM mapping supported by C, O, and Ni quantification based on EELS. The related data, shown in Figures 3, S1, and S2, confirm significant rearrangements of pristine NiO particles after the subsequent thermal treatments. Accordingly, SEM, HAADF-STEM and ZL-EFTEM imaging of bare NiO (Figure 3a, b, and c, respectively) reveal aggregates with size ranging from about 100 nm to about 5  $\mu\text{m}$  of nanometric grains (approximately between 5 and 20 nm), while elemental mapping (Figure 3d and e as well as Figure S1a and b in the Supplementary material) and HRTEM analysis (Figure 3f) show the expected homogenous distribution of Ni and O over the specimen and indicate a crystal structure in full agreement with the XRD patterns (ICSD # 9866; see Figure S2a), as clearly evidenced by the results of the fast Fourier transform (FFT, Figure 3f inset). Sucrose and NiO oxide reduction under an Ar flow (step 1) yields to Ni particles embedded in a carbon matrix including residual O traces (below 5 wt.%). In detail, SEM, HAADF-STEM, and EFTEM analyses (Figures 3g–k) reveal nickel metal particles and clusters mostly ranging from 10 nm to a few micrometers, which are surrounded by a significant amount of carbon, that is, between 54 and 62 wt.% according to SEM-EDS and EELS (see Figures S1c, d, and S2a in the Supplementary material). HRTEM imaging of a Ni grain enclosed in a carbon shell indicates the crystalline cubic structure with  $Fm\bar{3}m$  space group (ICSD # 260169; Figure 3l) for the core and an amorphous nature for the outer layer, thereby suggesting a microstructure at the nanoscale consistent with the powder XRD data (see Figure 2a). Hence, controlled oxidation of the Ni core (step 2) gives rise to a NiO@C material with similar morphological characteristic features to those of pristine NiO, in spite of an expected slight growth of the primary oxide grains forming the aggregates up to values approximately between 10 and 50 nm due to the thermal treatments (see the SEM, HAADF-STEM, and ZL-TEM images of Figure 3m, n, and o). Low carbon content is revealed by SEM-EDS (below 4 wt.%, Figure S1 in the

Supplementary material) along with the absence of a clear edge for carbon in the EEL spectra (Figure S2 in the Supplementary material), thus confirming the more accurate estimation by XRD and TGA data (below 4 wt.%). Moreover, EFTEM elemental mapping and HRTEM imaging (Figure 3p–r) suggest partial segregation of amorphous carbon and NiO oxide aggregates with cubic crystal structure with  $Fm\bar{3}m$  space group (ICSD # 260169). It is worth mentioning that nanograin agglomeration in micrometric and/or submicrometric cluster may ensure a suitable tap density in the electrode and fast reaction kinetics due to short electron paths [7,48], while a low carbon content (below 4 wt.% in the composite) may lead to a relevant gravimetric capacity. Besides such promising morphological characteristics for an application in lithium-ion cells, the NiO@C electrode is expected to benefit from conductive Ni metal particles possibly enhancing the rate capability.

### Figure 3

The conversion process of NiO and NiO@C has been comparatively characterized by coupling CV and EIS measurements in three-electrode cells. Figure 4 reports the related voltammetry profiles upon 3 cycles and the Nyquist plots (Figure 4 insets) recorded at the OCV and after each discharge/charge cycle (working electrode in the charged condition). Both techniques reveal that the above-discussed structural and morphological modifications promoted by the synthetic strategy adopted in this work, lead to an improvement of the electrochemical activity and a stabilization of the electrode/electrolyte interphase. During the first voltammetry scan towards low potential, pristine NiO shows a minor cathodic peak at 0.8 V vs.  $\text{Li}^+/\text{Li}$  followed by a strong signal at 0.6 V vs.  $\text{Li}^+/\text{Li}$  (Figure 4a), while NiO@C exhibits only a peak at 0.6 vs.  $\text{Li}^+/\text{Li}$  (Figure 4b). These responses are attributed to the well-known displacement of nickel oxide by reduction to form metallic Ni embedded into a  $\text{Li}_2\text{O}$  matrix [9], as well as to the formation of a solid electrolyte interphase (SEI) [13]. Hence, both electrodes undergo reversible oxidation throughout the first scan towards high potential by electrochemical processes mostly occurring at

2.2 V vs. Li<sup>+</sup>/Li, although pristine NiO shows a further small peak at 1.4 V vs. Li<sup>+</sup>/Li [49]. During the subsequent cycles, the reduction peak of NiO and NiO@C shifts to higher potential, *i.e.*, to 1.1 and 1.3 V vs. Li<sup>+</sup>/Li, respectively, suggesting massive electrode rearrangements associated with the electrochemical conversion as already reported for transition metal oxide anodes [13]. Despite the similar CV response, NiO@C exhibits a significantly lower polarization indicating improved electrode kinetics, which are further demonstrated by EIS (Figure 4 insets). The EIS measurements show for the pristine NiO electrode at OCV an electrode/electrolyte interphase represented by a medium-high frequency semicircle with a resistance of about 22 Ω, initially decreasing after the 1<sup>st</sup> cycle, and then increasing to about 30 Ω (inset of Figure 4a). Such increase of the resistance might indicate microstructural reorganization within the electrodes as well as a gradual growth and modification of the SEI layer [13]. On the other hand, the EIS reveals a lower resistance for NiO@C the OCV compared to the pristine NiO (about 17 Ω), and less relevant rise upon 3 CV cycles (to about 20 Ω), thereby suggesting improved electronic conductivity due to the carbon traces and beneficial effects on the electrode/electrolyte interphase (compare insets of Figure 4a and Figure 4b).

#### Figure 4

Therefore, both CV and EIS show that the two-step coating improves the electrochemical activity of nickel oxide by leading to a fast and reversible conversion reaction. Such an improvement is further revealed by comparative cycling tests at a C/5 rate of the bare nanopowder, the metal-carbon precursor, and the final composite (Figure 5a and b, 1C = 718 mA g<sup>-1</sup>). The first discharge of NiO and NiO@C, respectively, reveals plateaus at about 0.6 and 0.7 V leading to capacities of 970 and 1310 mAh g<sup>-1</sup> partially ascribed to the SEI formation [7], that is, a cell response in full agreement with CV (Figure 4). The subsequent charge evolves within a wide voltage range and is characterized by a plateau at about 2.2 and 2.1 V, according to the remarkable hysteresis of conversion materials [9], with reversible capacities of 690 and 820 mAh g<sup>-1</sup> for the

pristine and C-coated electrodes, respectively. Moreover, pristine NiO exhibits a further minor activity at about 0.8 V during discharge and at 1.4 V during charge as observed by CV (compare Figure 4a and Figure 5a). A minor contribution of carbon to the lithium exchange by insertion at low voltage might partially account for the higher reversible capacity of NiO@C with respect to the theoretical capacity of NiO (i.e., 718 mAh g<sup>-1</sup>) [23]. In addition, the improved charge transfer kinetics of NiO@C compared to pristine NiO (Figure 3 insets) may reasonably enhance the electrochemical conversion, leading to a lower cell polarization and improved cycling ability. Literature data [50] also indicate the pseudo-capacitive behavior of NiO as an additional boost for the delivered capacity above the theoretical value (718 mAh g<sup>-1</sup>). On the other hand, the Ni@C synthesis' intermediate shows a modest reversible electrochemical activity (about 100 mAh g<sup>-1</sup>) mainly due to lithium (de)insertion into the lowly crystalline carbon of Ni@C, beside first-cycle electrolyte decomposition at low voltage. Although both NiO and NiO@C exhibit reversible displacement upon three cycles, Figure 5b reveal an abrupt failure of NiO after 10 cycles, and much improved capacity retention and coulombic efficiency for NiO@C. Furthermore, both the voltammetry curves (Figure 4) and the galvanostatic profiles (Figure 5a) show that the electroreduction processes of NiO@C occur at a lower voltage than that of bare NiO, that is, about 1.3 V for the former and about 1.1 V for the latter after the first cycle. Such a shift of the reaction potentials towards higher value after the two-step treatment might reflect an improvement of the charge transfer at the electrode/electrolyte interphase leading to a decrease in cell polarization [51], as suggested by EIS measurements (Figure 4 insets) indicating a decrease in interphase resistance from about 30 Ω to about 20 Ω. Hence, the Figure 5b reveals a fast capacity fade down to about 100 mAh g<sup>-1</sup> for bare NiO, while NiO@C exhibits a much more stable behavior with a reversible capacity of 580 mAh g<sup>-1</sup> after 50 cycles and satisfactory coulombic efficiency.

Therefore, our results suggest a crucial role of the synthesis pathway in enhancing the electrochemical response of metal oxide nanomaterials by providing improved electric contact

within the electrode [52], as indicated by the fast charge transfer at the electrode/electrolyte interphase of Figure 4, thereby improving the reversibility and kinetics of the conversion reaction (see Figure 5a and b). The rate capability of the NiO@C material has been assessed by performing cycling tests at increasing current rates. Figure 5c and d shows the related voltage profiles and capacity trend, respectively. The nanocomposite anode displays a moderate polarization increasing by raising the current (Figure 5c) and reversible capacities of about 910, 860, 770, 690, 610, 510, and 390 mAh g<sup>-1</sup> at C/10, C/8, C/5, C/3, C/2, 1C, and 2C rates, respectively. This promising rate capability might be ascribed to the carbon traces (below 4 wt. %) as well as to the presence of conductive nickel (3–4 wt.%) [53]. However, the material exhibits a capacity fade as the current is lowered down to C/10 rate at the 36<sup>th</sup> cycle, with a final value of about 730 mAh g<sup>-1</sup> at the 40<sup>th</sup> cycle most likely attributed to partially irreversible rearrangement of the electrode material during conversion process, as indeed observed by the cycling test in Figure 4 [40,43].

### Figure 5

NiO-based anodes have been widely investigated elsewhere, revealing very promising performances in lithium half-cells with regard to the reversible capacity, cycling stability, and rate capability [26,29,54,30–37]. On the other hand, half-cell investigations might underestimate adverse electrochemical characteristics of the anode that affect the response in full lithium-ion array. Although conversion electrodes may deliver remarkable specific capacity values at high current rates, the huge voltage hysteresis, the wide working potential, and the unstable voltage typically require a careful tuning of the negative-to-positive (N/P) ratio as well as of the cycling conditions. Accordingly, several doubts have been raised on their possible applicability in lithium-ion batteries mostly owing to the large irreversible capacity loss, poor energy efficiency, low full-cell working voltage, and gradual microstructural changes that occur in the anode during cycling [5,13]. In this regard, the study in the lithium-ion cell may provide further insight on the electrode behavior and reveal practical issues not detected by using the electrode with lithium-metal in half-

cell [4,5]. Accordingly, we have investigated NiO@C in a full cell with the  $\text{LiNi}_{1/3}\text{Co}_{1/3}\text{Mn}_{1/3}\text{O}_2$  cathode. Prior to cell assembly, the anode has been electrochemically activated in a lithium-metal cell in order to mitigate the capacity loss during the first, partially irreversible cycle as described in the Experimental section. Figure 6 reports the NiO@C/NCM battery response in terms of voltage profile (panel a) and cycling behavior (panel b) at a constant current of  $C/2$  rate referred to the cathode mass (where  $1C$  is arbitrarily set at  $170 \text{ mA g}_{\text{cathode}}^{-1}$ ). During the first cycle, the cell delivers about  $160 \text{ mAh g}_{\text{cathode}}^{-1}$  in spite of an irreversible capacity of about  $67 \text{ mAh g}_{\text{cathode}}^{-1}$  corresponding to a coulombic efficiency of about 70%, which indicates oxidative electrolyte decomposition possibly related to the formation of a passivation layer over the positive electrode (see Figure 6a inset) [55]. Afterwards, the voltage signature stably reflects the combination of reversible  $\text{Li}^+$  exchange by conversion process at the anode and (de)intercalation at the cathode, thus leading to sloped plateaus within the range from 1.5 to 4.3 V which are centered at about 2.5 V (see Figure 6a). Accordingly, the NiO@C/NCM battery shows a reversible capacity slightly increasing to almost  $170 \text{ mAh g}_{\text{cathode}}^{-1}$  over the first 30 cycles with a steady-state coulombic efficiency above 99%, and then slowly decreasing to about  $140 \text{ mAh g}_{\text{cathode}}^{-1}$  after 80 cycles (ca. 88% of the initial value) due to a decrease in coulombic efficiency to about 97% (Figure 6b), and a gradual decay of the average voltage (Figure 6a).

The electrochemical behavior of the anode material and its effect on the lithium-ion battery performance is further elucidated by cycling and impedance measurements performed in a three-electrode cells, using NCM and NiO@C electrodes, and lithium metal as the reference electrode (third electrode). The cycling tests of the full cell have been performed using two electrodes, namely NCM and NiO@C, as already described in Figure 6a and b, while the responses of NCM and NiO@C electrodes during full-cell operation have been monitored by the support of the additional lithium reference electrode. Figure 6c-f reports the voltage profiles of the NiO@C/NCM cell (blue curve) cycled at a  $C/2$  rate ( $1C = 170 \text{ mAh g}_{\text{cathode}}^{-1}$ ) within a voltage range between

anode and cathode of 0.8 – 4.3 V as a function of time at the 1<sup>st</sup>, 10<sup>th</sup>, 50<sup>th</sup>, and 80<sup>th</sup> cycles. The potentials of NiO@C and NCM vs. Li<sup>+</sup>/Li monitored through the lithium electrode upon cycling are also reported in Figure 6c-f (purple and red colors, respectively). This cell setup allows a clear observation of the effects of the abovementioned change in cell balance on the characteristic voltage curve of the lithium-ion battery. Accordingly, the measurement reveals that the voltage decay of the cell actually reflects a gradual increase in potential of the negative electrode, that is, a progressive anode de-lithiation during cycling, which leads to a raise in potential of the positive electrode up to full-charge values exceeding 5 V vs. Li<sup>+</sup>/Li after 50 cycles. This phenomenon may be ascribed to irreversible parasitic processes occurring in the cell besides the Li-intercalation at the cathode and NiO conversion at the anode [23]. Notably, a remarkable cycle life may be achieved by ensuring coulombic efficiency values approaching 100% [56] or a suitable compensation of the irreversible capacity losses occurring at the anode side [57]. It worth considering that the wide working potential window of metal oxide anodes alongside a relevant hysteresis between charge and discharge may further magnify this gradual cell unbalancing [9,13,23].

### Figure 6

Impedance spectra of the NiO@C/NCM cell shed light on the evolution of the cathode and anode interphases during cycling. Indeed, EIS measurements of the full-cell have been performed at the OCV and after the 1<sup>st</sup>, 10<sup>th</sup>, 50<sup>th</sup>, and 80<sup>th</sup> cycle at the charged state (Figure 6g–j shows the related Nyquist plots). The obtained data have been modelled by the  $R_e(R_{(hf)1}Q_{(hf)1})(R_{(hf)2}Q_{(hf)2})(R_{(lf)}Q_{(lf)})$  equivalent circuit (see Table 2) and analyzed by an NLLS approach [58]. This circuit takes into account the electrolyte resistance ( $R_e$ ) and several resistive and pseudocapacitive elements that simulate the cell response within the investigated frequency range, thus enabling the study of various kinetic processes attributable to the NiO@C and NCM electrodes. In detail, the  $(R_{(hf)i}Q_{(hf)i})$  sub-circuit ( $i = 1, 2$ ) reflects the response of the cell at high-

medium frequency (herein briefly indicated as high-frequency region), occurring as a small semicircle in the Nyquist plots of Figure 6g–j, while the  $(R_{(lf)}Q_{(lf)})$  sub-circuit describes the large semicircle at medium-low frequency (herein briefly indicated as low-frequency region). Further spectra of the NiO@C and NCM electrodes performed employing the additional lithium reference probe (Figure S3a, c, e, g, and i for Li/NiO@C side and Figure S3b, d, f, h, and j for Li/NMC side) suggest a characteristic low-frequency response for NiO@C and NCM, that is, a Warburg-type diffusion for the former and a slow charge transfer for the latter after the 1<sup>st</sup> cycle, as well as an high-frequency region mostly reflecting the lithium passivation [59–61]. It is noteworthy that such a high charge transfer resistance at the cathode is in full agreement with the expected low Li<sup>+</sup> content in the NCM lattice in charged condition [59]. Based on these observations, we can attribute the  $(R_{(lf)}Q_{(lf)})$  sub-circuit (large low-frequency semicircle in Figure 6g–j) to the cathode charge transfer resistance and double layer capacitance. Besides, we ascribe the  $(R_{(hf)i}Q_{(hf)i})$  sub-circuit ( $i = 1, 2$ ) mostly to the passivation layers over the electrodes [59–61]. Negligible contribution of the anode charge transfer, and double layer capacitance in the low-frequency region is expected, considering the relatively small semicircles observed in the Nyquist plots of Figure 4. Notably, the EIS data at the OCV indicate the absence of charge transference in the cathode, which behaves as blocking electrode at about 3 V vs. Li<sup>+</sup>/Li [60] (see Figure 6g and Figure S3b in the Supplementary material), and overall high-frequency electrode/electrolyte interphase resistance of the order of 20  $\Omega$  in the lithium-ion cell ( $\Sigma R_{(hf)i}$  in Table 2). Galvanostatic cycling leads to an expected gradual increase of  $\Sigma R_{(hf)i}$  up to values approaching 60  $\Omega$  at the 80<sup>th</sup> cycle, which might be attributed to the growth of passivation layers over the electrodes owing to the abovementioned parasitic reactions [23], along with a raise of the cathode charge transfer resistance ( $R_{(lf)}$ ) from about 240  $\Omega$  after the 1<sup>st</sup> cycle to about 1200  $\Omega$  after the 80<sup>th</sup> cycle (see Table 1). This raise may be directly related to the increase in potential vs. Li<sup>+</sup>/Li of the positive electrode during cycling promoted by the concomitant change of the anode profile (see Figure 6c-f), which reflects a decreasing Li<sup>+</sup>

concentration in the NCM lattice at the charged state [59]. This trend suggests an increasing influence of the microstructural reorganization of the anode during the final stages of the cycling test leading to a progressive change of the cell balance [13]. Possible mitigation of this issue may be achieved by the optimization of the cell balance in terms of N/P ratio as well as by further improving the conversion oxide characteristics [13].

### Table 2

The effect of the electrode kinetics on the battery performance is further revealed by a rate capability test of a full NCM/NiO@C cell using the additional lithium probe reference to monitor the anode and the cathode potentials within the range from C/5 to 2C ( $1C = 170 \text{ mAh g}_{\text{cathode}}^{-1}$ ). The results are reported in Figure 7 as cycling trend (panel a), potential profiles of NiO@C and NMC electrodes vs. the lithium-metal reference (panels b and c, respectively), and voltage curves of the full NiO@C/NMC cell (panel d). The lithium-ion battery exhibits a decrease in capacity as the current increases, delivering about 178, 173, 161, 137, and 98  $\text{mAh g}_{\text{cathode}}^{-1}$  at current rates of C/5, C/3, C/2, 1C, and 2C, respectively; a current decrease back to the initial value of C/5 rate at the 51<sup>st</sup> cycle leads to a capacity of about 171  $\text{mAh g}_{\text{cathode}}^{-1}$ . An increase of cell polarization by current rising (see Figure 7d) reflects the expected overvoltage at the anode and cathode sides (see Figure 7b and c, respectively), while the modification of the electrode potential measured by the lithium probe suggests a gradual decrease in the  $\text{Li}^+$  concentration in both NiO@C and NCM during cycling, which is consistent with the results of Figure 6. In this regard, mitigation of parasitic  $\text{Li}^+$  consumption due to irreversible processes, occurring in the so-called “*rocking chair*” battery besides the (de)intercalation within the cathode and metal oxide conversion, is considered a crucial challenge that needs to be overcome for application [4,62,63].

In summary, the NiO@C anode exhibits a charging potential higher than that of graphite (mostly between 1.5 and 2.5 V vs.  $\text{Li}^+/\text{Li}$  compared to values ranging from 0.2 and 0.3 V vs.  $\text{Li}^+/\text{Li}$ , respectively) [64], which actually penalizes the working voltage of the lithium-ion cell as

compared to conventional batteries, although it may deliver a reversible capacity as high as 800 mAh g<sup>-1</sup> (compared to 372 mAh g<sup>-1</sup> for graphite), thereby decreasing the overall cell weight [4,63]. Accordingly, the NiO@C/NCM cell has a lower energy density than that of standard lithium-ion batteries. Moreover, the large potential hysteresis between charge and discharge has an adverse effect on the energy efficiency. On the other hand, the higher working voltage than that of graphite might mitigate possible lithium plating at the anode side, that is, a detrimental phenomenon with crucial impact on the safety level of cells and battery packs. Lithium electrodeposition on graphite is promoted by charging at low temperature and may lead to poor cycling performance, capacity fading and, in the worst-case scenario, to thermal runaways and uncontrolled exothermic reactions [65,66]. Therefore, high-voltage anodes might be more suitable than graphite for low-temperature applications [51].

### Figure 7

#### Conclusions

A NiO anode was prepared by a simple two-step pathway based on the reduction of oxide nanoparticles to metallic Ni embedded into a carbon matrix and subsequent mild oxidation of the metallic core. A comprehensive structural, compositional and morphological investigation revealed NiO grains between 10 and 50 nm forming aggregates ranging from about 100 nm to about 5 μm, as well as metallic Ni particles (3–4 wt.%) with crystallite size of the order of 100 nm and C traces (below 4 wt.%). The resulting NiO@C nanocomposite showed high reactivity in the cell, exchanging lithium ions by a conversion process mostly occurring at 1.3 V vs. Li<sup>+</sup>/Li during discharge and at 2.2 V vs. Li<sup>+</sup>/Li during charge. Preliminary results indicated that the two-step treatment remarkably enhances the characteristics of the metal oxide leading to a composite electrode delivering almost 800 mAh g<sup>-1</sup> at a C/5 rate. In particular, the material exhibited a higher specific capacity, faster kinetics at the electrode/electrolyte interphase, and a significantly longer cycle life than the pristine nano-powder. Accordingly, a suitable rate capability within the current

range from C/10 to 2C suggested possible application of the electrode in lithium-ion batteries. Therefore, a full-cell was assembled by coupling the NiO@C anode with a LiNi<sub>1/3</sub>Co<sub>1/3</sub>Mn<sub>1/3</sub>O<sub>2</sub> cathode, and it was studied by galvanostatic cycling at a C/2 rate as referred to the cathode, corresponding to 85 mA g<sup>-1</sup>. The NiO@C/NCM battery operated at about 2.5 V through sloped curves within the wide window from 1.5 to 4.3 V by delivering about 160 mAh g<sub>cathode</sub><sup>-1</sup> with reversibility and coulombic efficiency suitable to ensure about 80 cycles. Electrochemical measurements monitoring the potential vs. Li<sup>+</sup>/Li of anode and cathode revealed a gradual decrease in Li<sup>+</sup> concentration in both electrodes ascribable to parasitic processes leading to a progressive increase in interphase resistance. These changes yielded to a decrease in the average voltage of the cell during the cycling process. Although the straightforward two-step technique may might facilitate a possible application of conversion anodes, our results on full cell highlighted the issues still hindering a transition of conversion metal oxides for the laboratory to the market, which might be underestimated in the various works focusing on the synthesis, characterization, and tests in half cell. These results clarified the actual behavior of an enhanced nanostructured metal oxide anode in a lithium-ion battery, thereby providing valuable electrochemical contribute for further debating the applicability of the conversion anodes.

### **Acknowledgments**

This work was founded by “Fondo di Ateneo per la Ricerca Locale (FAR) 2019”, “Fondo per l’Incentivazione della Ricerca (FIR) 2018” University of Ferrara and performed within the project “Accordo di Collaborazione Quadro 2015” between University of Ferrara and Sapienza University of Rome. PRS acknowledges funding from The Royal Academy of Engineering (CIET1718/59).

### **References**

- [1] B. Scrosati, J. Hassoun, Y.-K. Sun, Lithium-ion batteries. A look into the future, *Energy Environ. Sci.* 4 (2011) 3287. doi:10.1039/c1ee01388b.

- [2] V. Etacheri, R. Marom, R. Elazari, G. Salitra, D. Aurbach, Challenges in the development of advanced Li-ion batteries: a review, *Energy Environ. Sci.* 4 (2011) 3243. doi:10.1039/c1ee01598b.
- [3] M. Lazzari, A cyclable lithium organic electrolyte cell based on two intercalation electrodes, *J. Electrochem. Soc.* 127 (1980) 773. doi:10.1149/1.2129753.
- [4] D. Di Lecce, R. Verrelli, J. Hassoun, Lithium-ion batteries for sustainable energy storage: recent advances towards new cell configurations, *Green Chem.* 19 (2017) 3442–3467. doi:10.1039/C7GC01328K.
- [5] V. Aravindan, Y.-S. Lee, S. Madhavi, Research progress on negative electrodes for practical Li-ion batteries: beyond carbonaceous anodes, *Adv. Energy Mater.* 5 (2015) 1402225. doi:10.1002/aenm.201402225.
- [6] J. Hassoun, P. Ochal, S. Panero, G. Mulas, C. Bonatto Minella, B. Scrosati, The effect of CoSn/CoSn<sub>2</sub> phase ratio on the electrochemical behaviour of Sn<sub>40</sub>Co<sub>40</sub>C<sub>20</sub> ternary alloy electrodes in lithium cells, *J. Power Sources.* 180 (2008) 568–575. doi:10.1016/j.jpowsour.2008.01.059.
- [7] J. Hassoun, B. Scrosati, Review—Advances in anode and electrolyte materials for the progress of lithium-ion and beyond lithium-ion batteries, *J. Electrochem. Soc.* 162 (2015) A2582–A2588. doi:10.1149/2.0191514jes.
- [8] P. Poizot, S. Laruelle, S. Grugeon, L. Dupont, J.M. Tarascon, Nano-sized transition-metal oxides as negative-electrode materials for lithium-ion batteries, *Nature.* 407 (2000) 496–499. doi:10.1038/35035045.
- [9] J. Cabana, L. Monconduit, D. Larcher, M.R. Palacín, Beyond intercalation-based Li-ion batteries: the state of the art and challenges of electrode materials reacting through Conversion Reactions, *Adv. Mater.* 22 (2010) E170–E192. doi:10.1002/adma.201000717.
- [10] M. V. Reddy, G. V. Subba Rao, B.V.R. Chowdari, metal oxides and oxysalts as anode

- materials for Li ion batteries, *Chem. Rev.* 113 (2013) 5364–5457. doi:10.1021/cr3001884.
- [11] X. Guo, Y.-Z. Zhang, F. Zhang, Q. Li, D.H. Anjum, H. Liang, Y. Liu, C. Liu, H.N. Alshareef, H. Pang, A novel strategy for the synthesis of highly stable ternary SiO<sub>x</sub> composites for Li-ion-battery anodes, *J. Mater. Chem. A.* 7 (2019) 15969–15974. doi:10.1039/C9TA04062E.
- [12] P. Geng, S. Zheng, H. Tang, R. Zhu, L. Zhang, S. Cao, H. Xue, H. Pang, Transition metal sulfides based on graphene for electrochemical energy storage, *Adv. Energy Mater.* 8 (2018) 1703259. doi:10.1002/aenm.201703259.
- [13] D. Di Lecce, S. Levchenko, F. Iacoviello, D.J.L. Brett, P.R. Shearing, J. Hassoun, X-ray nano-computed tomography of electrochemical conversion in lithium-ion battery, *ChemSusChem.* 12 (2019) 3550 – 3561. doi:10.1002/cssc.201901123.
- [14] S. Brutti, J. Hassoun, B. Scrosati, C.-Y.Y. Lin, H. Wu, H.-W.W. Hsieh, A high power Sn-C/LiFePO<sub>4</sub> lithium ion battery, *J. Power Sources.* 217 (2012) 72–76. doi:10.1016/j.jpowsour.2012.05.102.
- [15] V. Aravindan, Y.-S. Lee, S. Madhavi, Best practices for mitigating irreversible capacity loss of negative electrodes in Li-ion batteries, *Adv. Energy Mater.* 7 (2017) 1602607. doi:10.1002/aenm.201602607.
- [16] S.H. Yu, S.H. Lee, D.J. Lee, Y.E. Sung, T. Hyeon, Conversion reaction-based oxide nanomaterials for lithium ion battery anodes, *Small.* 12 (2016) 2146–2172. doi:10.1002/smll.201502299.
- [17] A. Palmieri, N. Spinner, S. Zhao, W.E. Mustain, Explaining the role and mechanism of carbon matrices in enhancing reaction reversibility of metal oxide anodes for high performance Li ion batteries, *Carbon* 130 (2018) 515–524. doi:10.1016/j.carbon.2018.01.059.
- [18] X. Sun, C. Yan, Y. Chen, W. Si, J. Deng, S. Oswald, L. Liu, O.G. Schmidt, Three-

- dimensionally “curved” NiO nanomembranes as ultrahigh rate capability anodes for Li-ion batteries with long cycle lifetimes, *Adv. Energy Mater.* 4 (2014) 1300912. doi:10.1002/aenm.201300912.
- [19] J.S. Cho, S.Y. Lee, H.S. Ju, Y.C. Kang, Synthesis of NiO nanofibers composed of hollow nanospheres with controlled sizes by the nanoscale Kirkendall diffusion process and their electrochemical properties, *ACS Appl. Mater. Interfaces.* 7 (2015) 25641–25647. doi:10.1021/acsami.5b08793.
- [20] C. Liu, C. Li, K. Ahmed, Z. Mutlu, C.S. Ozkan, M. Ozkan, Template free and binderless NiO nanowire foam for Li-ion battery anodes with long cycle life and ultrahigh rate capability, *Sci. Rep.* 6 (2016) 29183. doi:10.1038/srep29183.
- [21] S. Hwan Oh, J.-S. Park, M. Su Jo, Y.C. Kang, J.S. Cho, Design and synthesis of tube-in-tube structured NiO nanobelts with superior electrochemical properties for lithium-ion storage, *Chem. Eng. J.* 347 (2018) 889–899. doi:10.1016/j.cej.2018.04.156.
- [22] Q. Wang, J. Xu, G. Shen, Y. Guo, X. Zhao, Y. Xia, H. Sun, P. Hou, W. Xie, X. Xu, Large-scale carbon framework microbelts anchoring ultrafine SnO<sub>2</sub> nanoparticles with enhanced lithium storage properties, *Electrochim. Acta.* 297 (2019) 879–887. doi:10.1016/j.electacta.2018.11.175.
- [23] D. Di Lecce, R. Verrelli, D. Campanella, V. Marangon, J. Hassoun, A new CuO-Fe<sub>2</sub>O<sub>3</sub>-mesocarbon microbeads conversion anode in a high-performance lithium-ion battery with a Li<sub>1.35</sub>Ni<sub>0.48</sub>Fe<sub>0.1</sub>Mn<sub>1.72</sub>O<sub>4</sub> spinel cathode, *ChemSusChem.* 10 (2017) 1607–1615. doi:10.1002/cssc.201601638.
- [24] G. Zhou, J. Ma, L. Chen, Selective carbon coating techniques for improving electrochemical properties of NiO nanosheets, *Electrochim. Acta.* 133 (2014) 93–99. doi:10.1016/j.electacta.2014.03.161.
- [25] C. Xu, J. Sun, L. Gao, Large scale synthesis of nickel oxide/multiwalled carbon nanotube

- composites by direct thermal decomposition and their lithium storage properties, *J. Power Sources*. 196 (2011) 5138–5142. doi:10.1016/j.jpowsour.2011.02.001.
- [26] X. Liu, S.W. Or, C. Jin, Y. Lv, C. Feng, Y. Sun, NiO/C nanocapsules with onion-like carbon shell as anode material for lithium ion batteries, *Carbon* 60 (2013) 215–220. doi:10.1016/j.carbon.2013.04.014.
- [27] S.-H. Park, W.-J. Lee, Coaxial carbon nanofiber/NiO core–shell nanocables as anodes for lithium ion batteries, *RSC Adv.* 5 (2015) 23548–23555. doi:10.1039/C4RA15147J.
- [28] L. Zhou, H. Xu, H. Zhang, J. Yang, S. B. Hartono, K. Qian, J. Zou, C. Yu, Cheap and scalable synthesis of  $\alpha$ -Fe<sub>2</sub>O<sub>3</sub> multi-shelled hollow spheres as high-performance anode materials for lithium ion batteries, *Chem. Commun.* 49 (2013) 8695. doi:10.1039/c3cc43867h.
- [29] X. Zhang, Q. Huang, M. Zhang, M. Li, J. Hu, G. Yuan, Pine wood-derived hollow carbon fibers@NiO@rGO hybrids as sustainable anodes for lithium-ion batteries, *J. Alloys Compd.* 822 (2020) 153718. doi:10.1016/j.jallcom.2020.153718.
- [30] W. Jae, J. Song, J.J. Hong, J. Kim, Raspberry-like hollow Ni/NiO nanospheres anchored on graphitic carbon sheets as anode material for lithium-ion batteries, *J. Alloys Compd.* 805 (2019) 957–966. doi:10.1016/j.jallcom.2019.07.192.
- [31] C. Wang, L. Zhang, Y. Dou, L. Hencz, L. Jiang, M. Al-Mamun, P. Liu, S. Zhang, D. Wang, H. Zhao, Transition metal (Fe, Co, Mn) boosting the lithium storage of the multishelled NiO anode, *Energy Technol.* (2020) 2000008. doi:10.1002/ente.202000008.
- [32] Q. Zhang, F. Liu, P. Gao, P. Zhao, H. Guo, L. Wang, Z. Li Wan, Three-dimensional hollow NiO/NC nanoparticles for high-performance lithium ion batteries, *Mater. Lett.* 268 (2020) 127366. doi:10.1016/j.matlet.2020.127366.
- [33] J. Zhu, G. Cao, Y. Li, X. Xi, Z. Jin, B. Xu, W. Li, Efficient utilisation of rod-like nickel oxalate in lithium-ion batteries: A case of NiO for the anode and LiNiO<sub>2</sub> for the cathode,

Scr. Mater. 178 (2020) 51–56. doi:10.1016/j.scriptamat.2019.10.051.

- [34] J. Jiang, J. Liu, Y. Chen, R. Sun, Y. Liu, Y. Yang, Y. Yang, G. Yang, Preparation of hierarchical hexagonal nanoplates NiO composite with microcrystalline graphite for highly reversible lithium storage, *J. Alloys Compd.* 815 (2020) 152333. doi:10.1016/j.jallcom.2019.152333.
- [35] L. Ma, S.-S. Lyu, Y. Dai, X.-Y. Pei, D.-C. Mo, Y.-X. Fu, Lithium storage properties of NiO/reduced graphene oxide composites derived from different oxidation degrees of graphite oxide, *J. Alloys Compd.* 810 (2019) 151954. doi:10.1016/j.jallcom.2019.151954.
- [36] X. Shi, S. Zhang, X. Chen, T. Tang, R. Klingeler, E. Mijowska, Ultrathin NiO confined within hollow carbon sphere for efficient electrochemical energy storage, *J. Alloys Compd.* 797 (2019) 702–709. doi:10.1016/j.jallcom.2019.05.147.
- [37] J. Fu, W. Kang, X. Guo, H. Wen, T. Zeng, R. Yuan, C. Zhang, 3D hierarchically porous NiO/Graphene hybrid paper anode for long-life and high rate cycling flexible Li-ion batteries, *J. Energy Chem.* 47 (2020) 172–179. doi:10.1016/j.jechem.2019.11.022.
- [38] B. Ng, X. Peng, E. Faegh, W.E. Mustain, Using nanoconfinement to inhibit the degradation pathways of conversion-metal oxide anodes for highly stable fast-charging Li-ion batteries, *J. Mater. Chem. A.* 8 (2020) 2712–2727. doi:10.1039/C9TA11708C.
- [39] Y. Huang, H. Yang, T. Xiong, D. Adekoya, W. Qiu, Z. Wang, S. Zhang, M.-S. Balogun, Adsorption energy engineering of nickel oxide hybrid nanosheets for high areal capacity flexible lithium-ion batteries, *Energy Storage Mater.* 25 (2020) 41–51. doi:10.1016/j.ensm.2019.11.001.
- [40] R. Verrelli, J. Hassoun, High-capacity NiO-(mesocarbon microbeads) conversion anode for lithium-ion battery, *ChemElectroChem.* 2 (2015) 988–994. doi:10.1002/celc.201500069.
- [41] X. Lv, J. Deng, B. Wang, J. Zhong, T.-K. Sham, X. Sun, X. Sun,  $\gamma$ -Fe<sub>2</sub>O<sub>3</sub>@CNTs anode materials for lithium ion batteries investigated by electron energy loss spectroscopy, *Chem.*

- Mater. 29 (2017) 3499–3506. doi:10.1021/acs.chemmater.6b05356.
- [42] Y. Wang, X. Guo, Z. Wang, M. Lü, B. Wu, Y. Wang, C. Yan, A. Yuan, H. Yang, Controlled pyrolysis of MIL-88A to Fe<sub>2</sub>O<sub>3</sub>@C nanocomposites with varied morphologies and phases for advanced lithium storage, *J. Mater. Chem. A* 5 (2017) 25562–25573. doi:10.1039/C7TA08314A.
- [43] R. Verrelli, R. Brescia, A. Scarpellini, L. Manna, B. Scrosati, J. Hassoun, A lithium ion battery exploiting a composite Fe<sub>2</sub>O<sub>3</sub> anode and a high voltage Li<sub>1.35</sub>Ni<sub>0.48</sub>Fe<sub>0.1</sub>Mn<sub>1.72</sub>O<sub>4</sub> cathode, *RSC Adv.* 4 (2014) 61855–61862. doi:10.1039/C4RA12598C.
- [44] L. Lutterotti, D. Chateigner, S. Ferrari, J. Ricote, Texture, residual stress and structural analysis of thin films using a combined X-ray analysis, *Thin Solid Films*. 450 (2004) 34–41. doi:10.1016/j.tsf.2003.10.150.
- [45] H.H. Wei, Q. Zhang, Y. Wang, Y.J. Li, J.C. Fan, Q.J. Xu, Y.L. Min, Baby diaper-inspired construction of 3D porous composites for long-term lithium-ion batteries, *Adv. Funct. Mater.* 28 (2018) 1704440. doi:10.1002/adfm.201704440.
- [46] S. Sasaki, K. Fujino, Y. Takéuchi, X-Ray determination of electron-density distributions in oxides, MgO, MnO, CoO, and NiO, and atomic scattering factors of their constituent atoms, *Proc. Japan Acad. Ser. B Phys. Biol. Sci.* 55 (1979) 43–48. doi:10.2183/pjab.55.43.
- [47] D. Rodic, V. Spasojevic, V. Kusigerski, R. Tellgren, H. Rundlof, Magnetic ordering in polycrystalline Ni<sub>x</sub>Zn<sub>1-x</sub>O Solid Solutions, *Phys. Status Solidi*. 218 (2000) 527–536. doi:10.1002/1521-3951(200004)218:2<527::AID-PSSB527>3.0.CO;2-I.
- [48] I. Hasa, J. Hassoun, S. Passerini, Nanostructured Na-ion and Li-ion anodes for battery application: A comparative overview, *Nano Res.* 10 (2017) 3942–3969. doi:10.1007/s12274-017-1513-7.
- [49] F. Zou, Y.-M. Chen, K. Liu, Z. Yu, W. Liang, S.M. Bhaway, M. Gao, Y. Zhu, Metal organic frameworks derived hierarchical hollow NiO/Ni/graphene composites for lithium and

- sodium storage, *ACS Nano*. 10 (2016) 377–386. doi:10.1021/acsnano.5b05041.
- [50] V. Aravindan, P. Suresh Kumar, J. Sundaramurthy, W.C. Ling, S. Ramakrishna, S. Madhavi, Electrospun NiO nanofibers as high performance anode material for Li-ion batteries, *J. Power Sources*. 227 (2013) 284–290. doi:10.1016/j.jpowsour.2012.11.050.
- [51] D. Di Lecce, R. Verrelli, J. Hassoun, New lithium ion batteries exploiting conversion/alloying anode and  $\text{LiFe}_{0.25}\text{Mn}_{0.5}\text{Co}_{0.25}\text{PO}_4$  olivine cathode, *Electrochim. Acta*. 220 (2016) 384–390. doi:10.1016/j.electacta.2016.10.067.
- [52] G. Chen, L. Yan, H. Luo, S. Guo, Nanoscale engineering of heterostructured anode materials for boosting lithium-ion storage, *Adv. Mater.* (2016) 7580–7602. doi:10.1002/adma.201600164.
- [53] Y. Fu, Z. Yang, X. Li, X. Wang, D. Liu, D. Hu, L. Qiao, D. He, Template-free synthesized Ni nanofoams as nanostructured current collectors for high-performance electrodes in lithium ion batteries, *J. Mater. Chem. A*. 1 (2013) 10002. doi:10.1039/c3ta11753g.
- [54] G. Li, Y. Li, J. Chen, P. Zhao, D. Li, Y. Dong, L. Zhang, Synthesis and research of egg shell-yolk NiO/C porous composites as lithium-ion battery anode material, *Electrochim. Acta*. 245 (2017) 941–948. doi:10.1016/j.electacta.2017.06.039.
- [55] M. Gauthier, T.J. Carney, A. Grimaud, L. Giordano, N. Pour, H.-H. Chang, D.P. Fenning, S.F. Lux, O. Paschos, C. Bauer, F. Maglia, S. Lupart, P. Lamp, Y. Shao-Horn, Electrode–electrolyte interface in Li-ion batteries: current understanding and new insights, *J. Phys. Chem. Lett.* 6 (2015) 4653–4672. doi:10.1021/acs.jpcllett.5b01727.
- [56] G.A. Elia, U. Ulissi, S. Jeong, S. Passerini, J. Hassoun, Exceptional long-life performance of lithium-ion batteries using ionic liquid-based electrolytes, *Energy Environ. Sci.* 9 (2016) 3210–3220. doi:10.1039/C6EE01295G.
- [57] G. Gabrielli, M. Marinaro, M. Mancini, P. Axmann, M. Wohlfahrt-Mehrens, A new approach for compensating the irreversible capacity loss of high-energy

- Si/C|LiNi<sub>0.5</sub>Mn<sub>1.5</sub>O<sub>4</sub> lithium-ion batteries, *J. Power Sources*. 351 (2017) 35–44. doi:10.1016/j.jpowsour.2017.03.051.
- [58] B.A. Boukamp, A Nonlinear Least Squares Fit procedure for analysis of immittance data of electrochemical systems, *Solid State Ionics*. 20 (1986) 31–44. doi:10.1016/0167-2738(86)90031-7.
- [59] D. Di Lecce, D. Campanella, J. Hassoun, Insight on the enhanced reversibility of a multimetal layered oxide for sodium-ion battery, *J. Phys. Chem. C*. 122 (2018) 23925–23933. doi:10.1021/acs.jpcc.8b07596.
- [60] D. Di Lecce, V. Gancitano, J. Hassoun, Investigation of Mn and Fe substitution effects on the characteristics of high-voltage LiCo<sub>1-x</sub>M<sub>x</sub>PO<sub>4</sub> ( x = 0.1, 0.4) cathodes prepared by sol-gel route, *ACS Sustain. Chem. Eng.* 8 (2020) 278–289. doi:10.1021/acssuschemeng.9b05325.
- [61] S. Wei, S. Inoue, D. Di Lecce, Z. Li, Y. Tominaga, J. Hassoun, Towards a highly performing lithium-metal battery with glyme solution and olivine cathode, *ChemElectroChem*. (2020) celc.202000272. doi:10.1002/celc.202000272.
- [62] B. Scrosati, Lithium Rocking Chair Batteries: An Old Concept?, *J. Electrochem. Soc.* 139 (1992) 2776. doi:10.1149/1.2068978.
- [63] D. Di Lecce, P. Andreotti, M. Boni, G. Gasparro, G. Rizzati, J.-Y. Hwang, Y.-K. Sun, J. Hassoun, Multiwalled carbon nanotubes anode in lithium-ion battery with LiCoO<sub>2</sub>, Li[Ni<sub>1/3</sub>Co<sub>1/3</sub>Mn<sub>1/3</sub>]O<sub>2</sub>, and LiFe<sub>1/4</sub>Mn<sub>1/2</sub>Co<sub>1/4</sub>PO<sub>4</sub> Cathodes, *ACS Sustain. Chem. Eng.* 6 (2018) 3225–3232. doi:10.1021/acssuschemeng.7b03395.
- [64] V.A. Sethuraman, L.J. Hardwick, V. Srinivasan, R. Kostecki, Surface structural disordering in graphite upon lithium intercalation/deintercalation, *J. Power Sources*. 195 (2010) 3655–3660. doi:10.1016/j.jpowsour.2009.12.034.
- [65] B.P. Matadi, S. Geniès, A. Delaille, C. Chabrol, E. de Vito, M. Bardet, J.-F. Martin, L.

Daniel, Y. Bultel, Irreversible capacity loss of Li-ion batteries cycled at low temperature due to an untypical layer hindering Li diffusion into graphite electrode, *J. Electrochem. Soc.* 164 (2017) A2374–A2389. doi:10.1149/2.0491712jes.

- [66] A. Friesen, F. Horsthemke, X. Mönnighoff, G. Brunklaus, R. Krafft, M. Börner, T. Risthaus, M. Winter, F.M. Schappacher, Impact of cycling at low temperatures on the safety behavior of 18650-type lithium ion cells: combined study of mechanical and thermal abuse testing accompanied by post-mortem analysis, *J. Power Sources.* 334 (2016) 1–11. doi:10.1016/j.jpowsour.2016.09.120.

## Table captions

**Table 1.** Results of Rietveld refinement of the XRD pattern of NiO@C in terms of space group, weight fraction, crystallite size, lattice parameter, unit cell volume of the crystalline NiO and Ni phases, along with good-of-fit (GOF,  $\sigma$ ) parameter and weighted-profile R factor ( $R_{wp}\%$ ).

**Table 2.** Results of NLLS analysis of EIS data on the NiO@C/NCM cell at the OCV and after the 1<sup>st</sup>, 10<sup>th</sup>, 50<sup>th</sup>, and 80<sup>th</sup> cycles at the charged state in terms of  $\chi^2$  parameter and electrode/electrolyte interphase resistance.  $\sum R_{(hf)i}/\Omega$  ( $i = 1, 2$ ) is the sum of interphase resistances at high-medium frequency (briefly high-frequency region) and  $R_{(lf)}/\Omega$  is the interphase resistance at medium-low frequency (briefly low-frequency region). Analysis performed by using the Boukamp software [58]. See the voltage profiles of the NiO@C/NCM full-cell in Figure 6c–f, and the corresponding Nyquist plots in Figure 6g–j. EIS Nyquist plots of Li/NMC and Li/NiO@C sides during full-cell cycling collected by the lithium reference probe are shown in Figure S3 of the Supplementary material.

## Figure captions

**Figure 1.** Schematic illustration of the two-step synthetic pathway. In detail: (step 1) sucrose precipitation on bare NiO followed by pyrolysis at 600 °C under an Ar flow; (step 2) mild oxidation of the Ni@C intermediate by heating at 380 °C under an air flow to form the NiO@C material.

**Figure 2.** (a) XRD patterns of pristine NiO, Ni@C (after step 1) and NiO@C (after step 2). The patterns have been indexed to the reference structures of NiO (ICSD # 9866), and Ni (ICSD # 260169) with space group  $Fm\bar{3}m$  (No. 225); see Table 1 reporting the Rietveld refinement results for NiO@C. (b) TGA under an air flow (50 mL min<sup>-1</sup>) at a heating rate of 10 °C min<sup>-1</sup> from 30 to 800 °C (mass percent on the left y-axis), with suggested reactions occurring in the sample and mass percent variation in inset.

**Figure 3.** Electron microscopy analyses of (a–f) bare NiO, (g–l) Ni@C, and (m–r) NiO@C powders. In detail: (a, g, and m) SEM images of the three samples (magnified views in the insets); (b, h, n) HAADF-STEM images; (c, i, and o) ZL-TEM images and (d and e, j and k, p and q) corresponding EFTEM elemental maps, showing the distribution of (d, j, and p) C + O (green and blue, respectively) and C + Ni (green and red); (f, l, and r) HRTEM images and corresponding fast Fourier transforms (FFTs) results indexed to the (f and r) ICSD # 9866 and (l) ICSD # 260169 reference structures.

**Figure 4.** CV and (insets) EIS Nyquist plots of (a) NiO and (b) NiO@C in three-electrode lithium half-cells. CV performed at 0.1 mV s<sup>-1</sup> within 0.01 – 2.8 V vs. Li<sup>+</sup>/Li. Impedance spectra recorded at the OCV and after 1, 2 and 3 full voltammetry cycles by applying an alternate voltage signal with amplitude of 10 mV in the 500 kHz – 100 mHz range.

**Figure 5.** (a and b) Cycling response of NiO, Ni@C and NiO@C in two-electrode half-cells at a C/5 rate (1C = 718 mA g<sup>-1</sup>) in terms of (a) voltage profiles and (b) cycling behavior. (c and d) Rate capability tests of NiO@C in a two-electrode half-cell at C/10, C/8, C/5, C/3, C/2, 1C, 2C

rates ( $1C = 718 \text{ mA g}^{-1}$ ), respectively, in terms of (c) voltage profiles and (d) cycling behavior. Voltage window: 0.01 – 2.8 V.

**Figure 6.** Electrochemical characterization of the NiO@C/NCM cell. In detail: (a–b) galvanostatic cycling at a rate of  $C/2$  in terms of (a) voltage profiles and (b) cycling behavior ( $1C = 170 \text{ mA g}_{\text{cathode}}^{-1}$ ); specific capacity referred to the NCM mass; galvanostatic-cycling voltage range controlled in the NiO@C/NMC cell: 0.8 – 4.3 V; prior to the full-cell assembling, the NiO@C anode has been electrochemically activated by performing 3 discharge/charge galvanostatic cycles in a T-type half-cell at a  $C/5$  rate from 0.01 to 2.8 V with final charge up to 2.2 V; (c–f) potential of anode and cathode vs.  $\text{Li}^+/\text{Li}$  as measured by a lithium-metal reference probe in the cell and corresponding voltage profile of the full cell (*i.e.*, cathode vs. anode) for the (c) 1<sup>st</sup>, (d) 10<sup>th</sup>, (e) 50<sup>th</sup>, and (f) 80<sup>th</sup> cycles; (g–j) experimental and simulated EIS Nyquist plots of the full cell at the (g) OCV and after the (g) 1<sup>st</sup>, (h) 10<sup>th</sup>, (i) 50<sup>th</sup>, and (j) 80<sup>th</sup> cycles at the charged state; EIS performed by applying an alternate voltage signal of 10 mV within the frequency range from 500 kHz to 20 mHz to the cell; simulation of the spectra has been carried out by NLLS analysis [58] according to the  $R_e(R_{(hf)1}Q_{(hf)1})(R_{(hf)2}Q_{(hf)2})(R_{(lf)}Q_{(lf)})$  equivalent circuit (see Table 2 for the related results in terms of  $\chi^2$  parameter and electrode/electrolyte interphase resistance); EIS Nyquist plots of either electrodes vs. a lithium-metal probe in the cell are shown in Figure S3 of the Supplementary material.

**Figure 7.** Results of a rate capability test within the current range from  $C/5$  to  $2C$  rates ( $1C = 170 \text{ mAh g}_{\text{cathode}}^{-1}$ ) in terms of (a) cycling trend, potential profiles of (b) NiO@C and (c) NMC vs.  $\text{Li}^+/\text{Li}$  as measured by a lithium-metal reference probe in the cell, and (d) voltage curves of the NiO@C/NMC cell. Specific capacity referred to the NCM mass for panels a, c, and d and to the NiO@C mass for panel b; galvanostatic-cycling voltage range controlled in the NiO@C/NMC cell: 0.8 – 4.3 V; prior to the full-cell assembling, the NiO@C anode has been electrochemically

activated by performing 3 discharge/charge galvanostatic cycles in a T-type half-cell at a C/5 rate from 0.01 to 2.8 V with final charge up to 2.2 V.

Phase	Space group	Weight fraction	(Crystallite size)/Å	a/Å	V/Å <sup>3</sup>	GOF (σ)	R <sub>wp</sub> %
NiO	<i>Fm</i> $\bar{3}$ <i>m</i> (No. 225)	0.96±0.02	340.1±0.3	4.1794(1)	73.006(8)	1.6	9
Ni	<i>Fm</i> $\bar{3}$ <i>m</i> (No. 225)	0.04±0.02	1400±100	3.5278(2)	43.905(7)		

**Table 1**

Cell condition	Equivalent circuit	$\chi^2$	$\sum R_{(hf)i}/\Omega$ (i = 1, 2)	$R_{(lf)}/\Omega$
OCV	$R_e(R_{(hf)1}Q_{(hf)1})(R_{(hf)2}Q_{(hf)2})Q_{(lf)}$	$1.8 \times 10^{-4}$	21±7	–
1 <sup>st</sup> cycle	$R_e(R_{(hf)1}Q_{(hf)1})(R_{(hf)2}Q_{(hf)2})(R_{(lf)}Q_{(lf)})$	$2.5 \times 10^{-4}$	22±10	238±8
10 <sup>th</sup> cycle	$R_e(R_{(hf)1}Q_{(hf)1})(R_{(hf)2}Q_{(hf)2})(R_{(lf)}Q_{(lf)})$	$2.6 \times 10^{-4}$	29±15	570±20
50 <sup>th</sup> cycle	$R_e(R_{(hf)1}Q_{(hf)1})(R_{(lf)}Q_{(lf)})$	$4.0 \times 10^{-4}$	42.5±0.5	790±30
80 <sup>th</sup> cycle	$R_e(R_{(hf)1}Q_{(hf)1})(R_{(hf)2}Q_{(hf)2})(R_{(lf)}Q_{(lf)})$	$5.2 \times 10^{-4}$	58±14	1260±40

**Table 2**

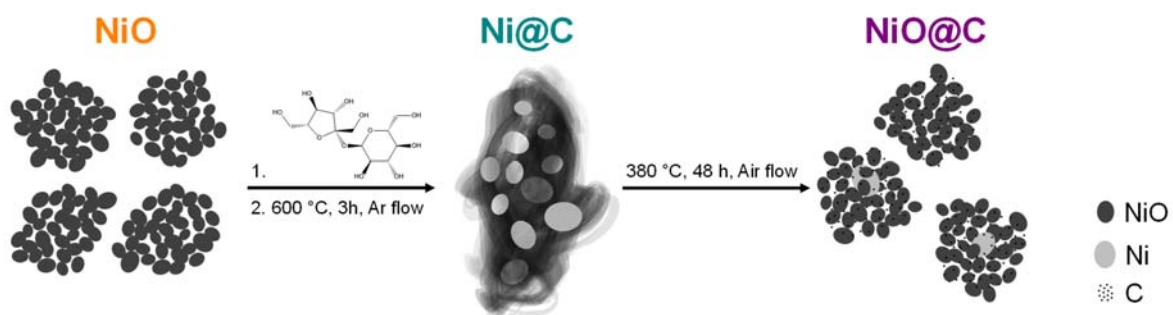


**Figure 1**

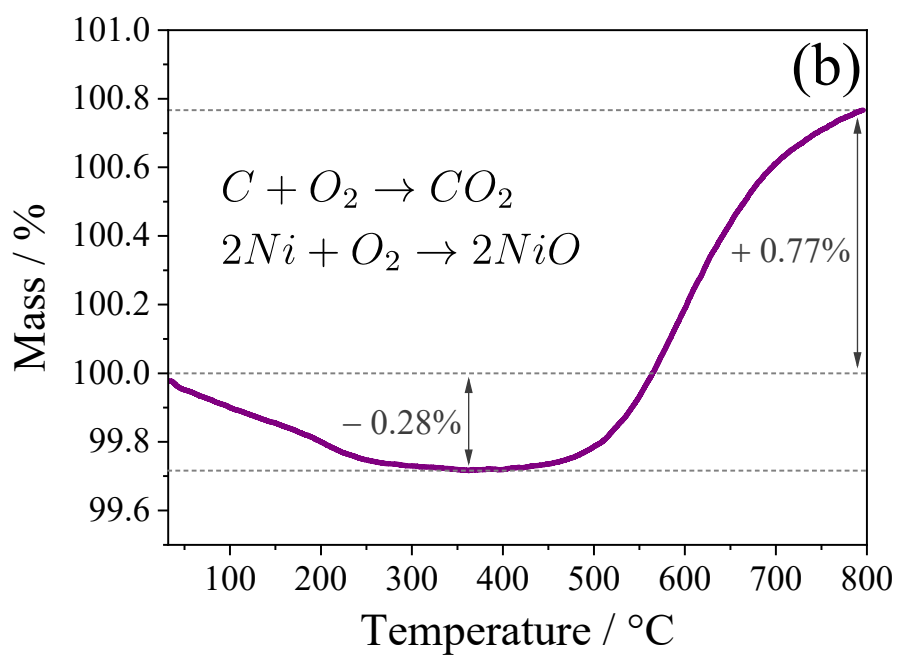
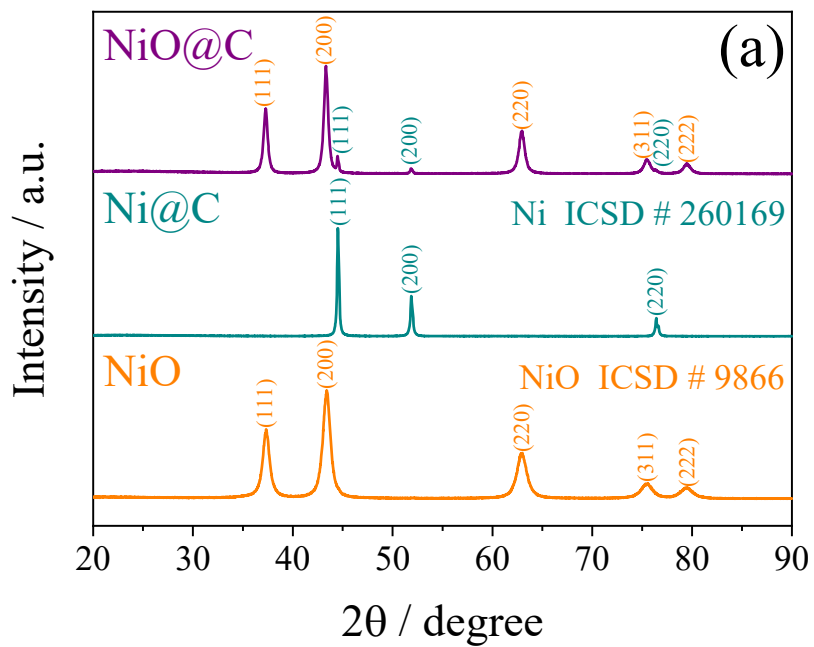


Figure 2

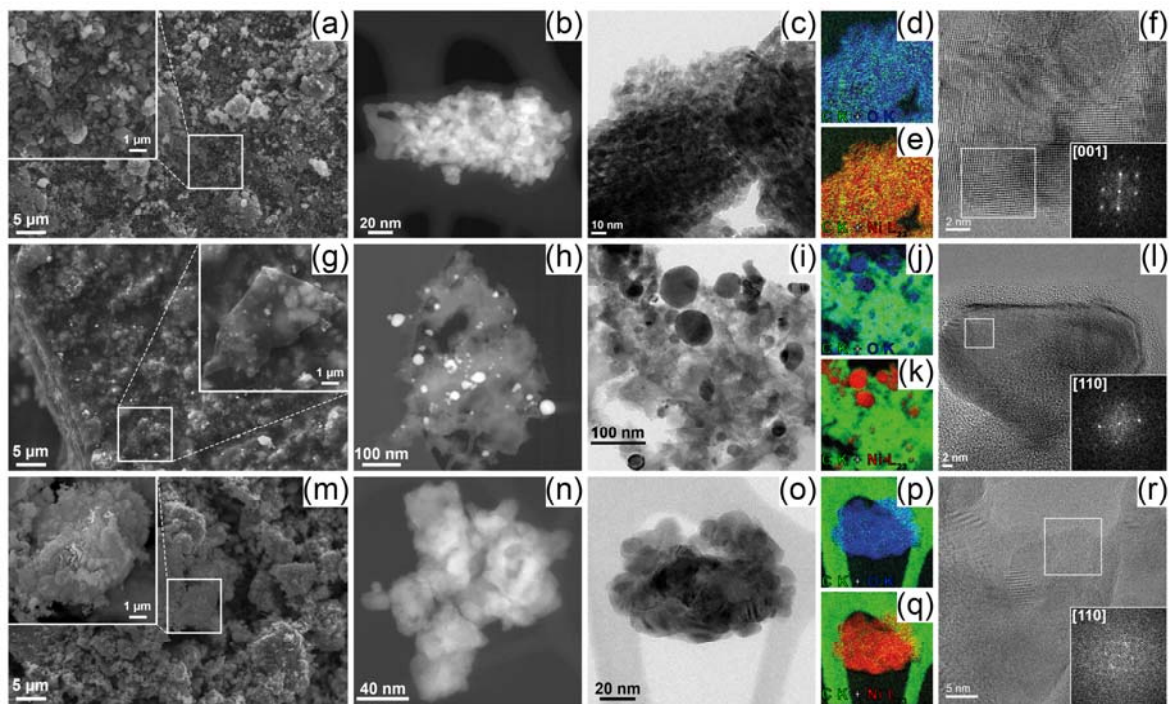
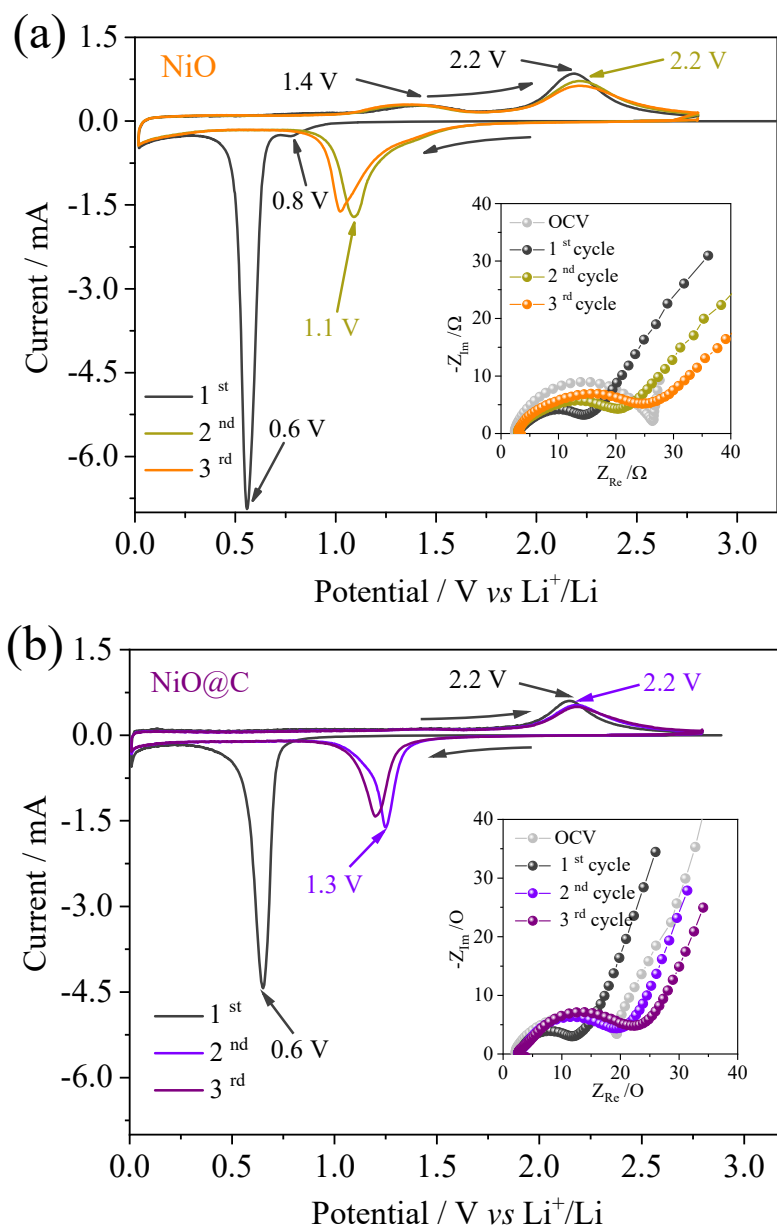


Figure 3



**Figure 4**

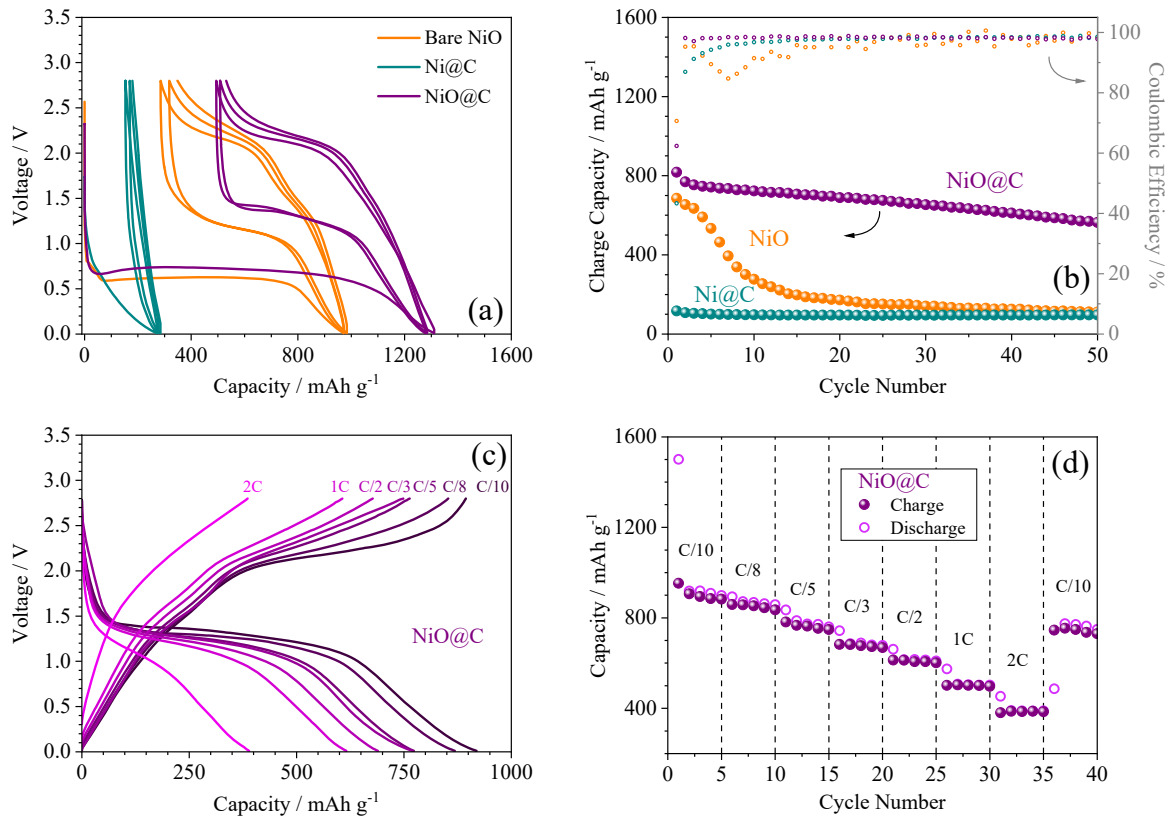


Figure 5

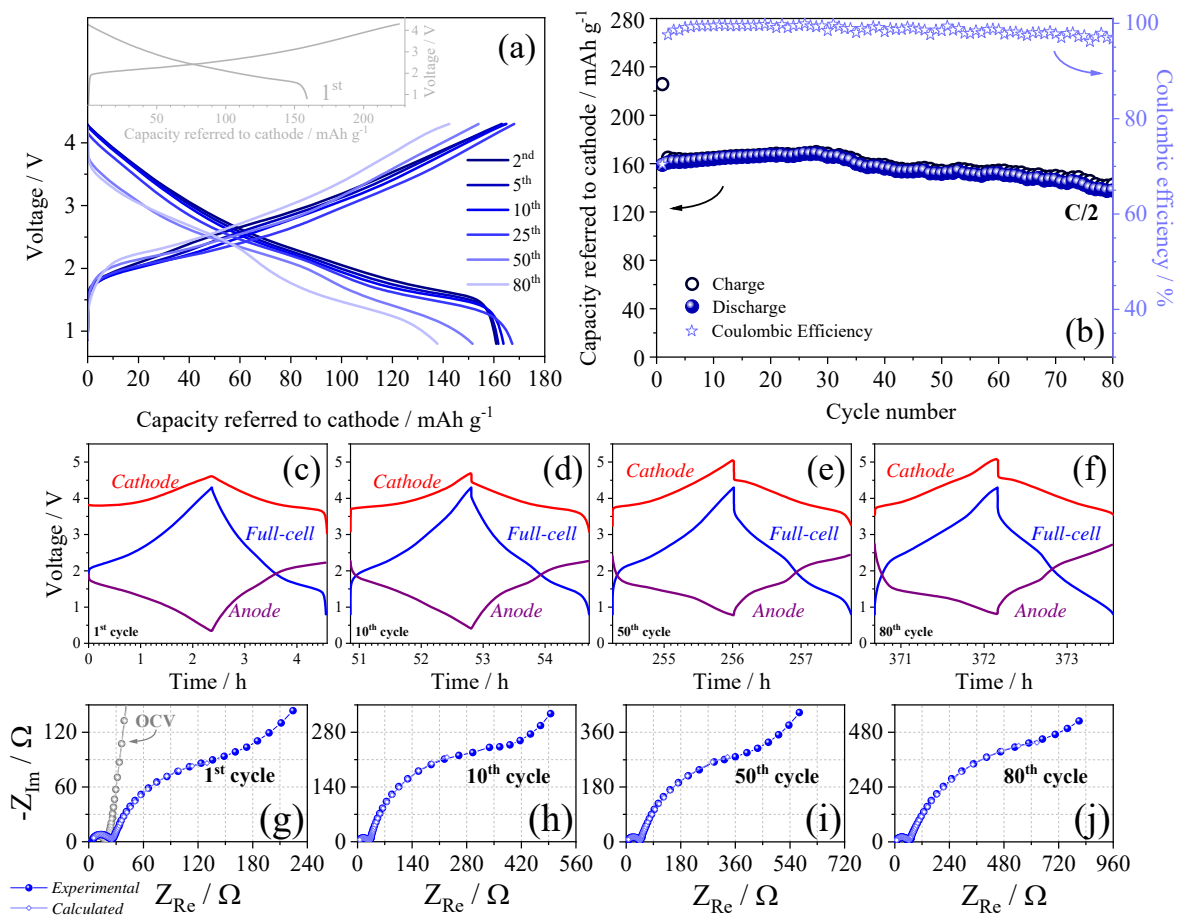


Figure 6

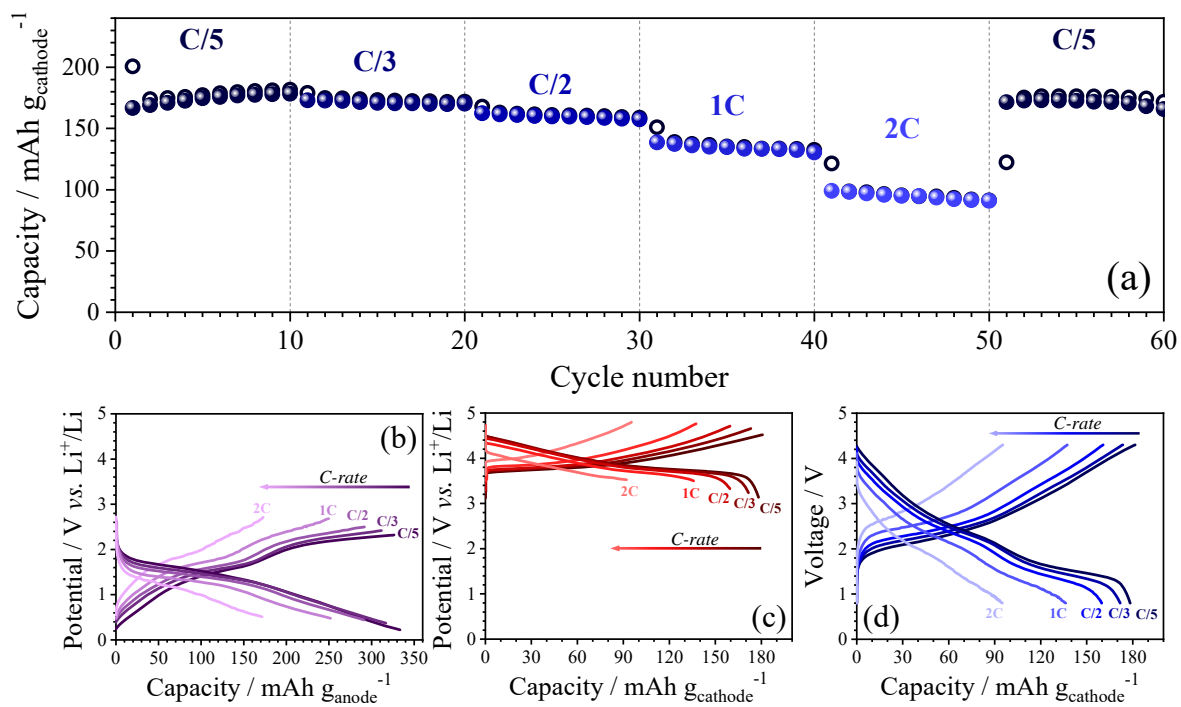


Figure 7